Aggregate-Forming Semi-Synthetic Chlorophyll Derivatives / $Ti_3C_2T_x$ MXene Hybrids for Photocatalytic Hydrogen Evolution

Yuanlin Li[a], Yanxiang Liu[a], Xiaoli Sun[a], Tianfang Zheng[a], Yohan Dall'Agnese[b], Chunxiang Dall'Agnese[a], Shin-ichi Sasaki[c,d], Hitoshi Tamiaki[c] and Xiao-Feng Wang[a,*]

[a] *Key Laboratory of Physics and Technology for Advanced Batteries (Ministry of Education), College of Physics, Jilin University, Changchun 130012, PR China*

[b] *Institute for Materials Discovery, University College London, London WC1E 7JE, United Kingdom*

[c] *Graduate School of Life Sciences, Ritsumeikan University, Kusatsu, Shiga 525-8577, Japan*

[d] *Nagahama Institute of Bio-Science and Technology, Nagahama, Shiga 526-0829, Japan*

*E-mail: xf_wang@jlu.edu.cn

HIGHLIGHTS

- Three different aggregate-forming chlorophyll derivatives are compared for hydrogen evolution.
- Highly efficient electron-hole separation through the exciton transfer in Chl aggregates.
- Chl@MXene-based photocatalytic system is developed.
- This work leads the direction in synthesizing Chls in Chl/MXene hybrid structure suitable for highly efficient photocatalytic HER.

GRAPHICAL ABSTRACT

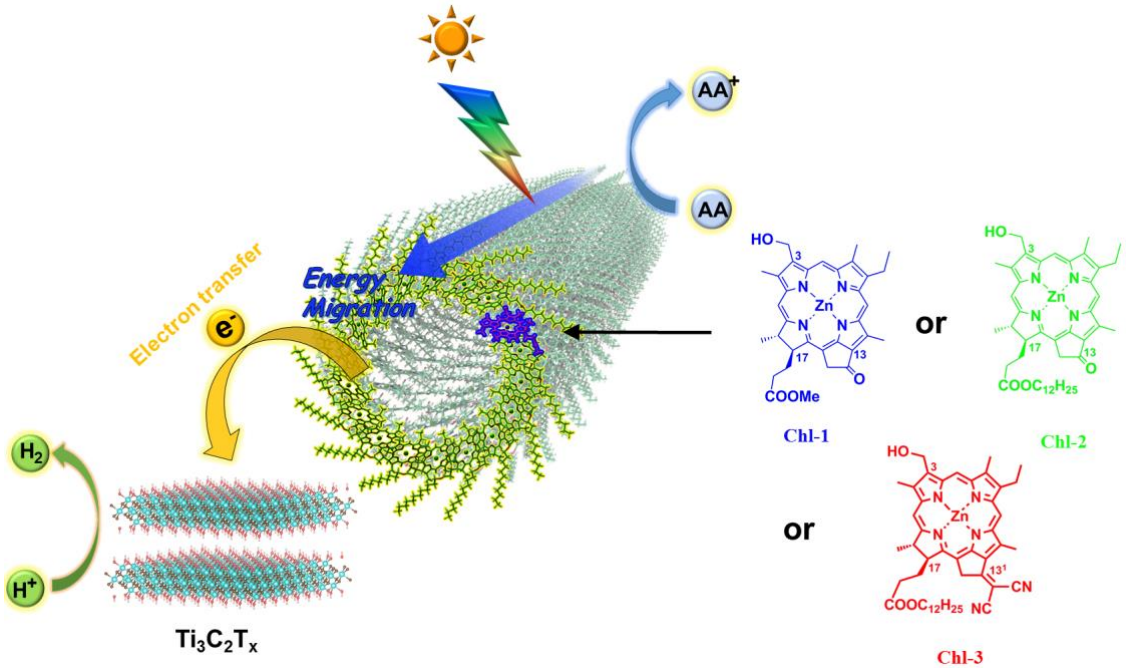

ABSTRACT

Chlorophylls (Chls) are the most abundant natural pigments having excellent opt-electrical and semi-conductive properties. $Ti_3C_2T_x$ MXene, one of the most extensively studied 2D noble metal-free co-catalyst, features outstanding electrochemical properties. This work compares three aggregate-forming chlorophyll derivatives (Chl-n; n = 1~3), namely, zinc methyl 3-devinyl-3-hydroxymethyl-pyropheophorbide-*a* (Chl-1), zinc dodecyl 3-devinyl-3-hydroxymethyl-pyropheophorbide-*a* (Chl-2) and zinc dodecyl 13^1-deoxo-3-devinyl-13^1-dicyanomethylene-3-hydroxymethyl-pyropheophorbide-*a* (Chl-3), as light-harvesting antenna pigments in the MXene-based photocatalytic system for hydrogen evolution under the white light illumination ($\lambda > 420$ nm). The hydrogen evolution reaction (HER) of these Chls depends on the peripheral substituent groups at the C13- and/or C17-positions of the chlorin macrocyclic π-system. Differences among these Chl-n sensitized $Ti_3C_2T_x$ MXene (Chl-n@$Ti_3C_2T_x$) are compared in terms of their light-harvesting ability, morphology, charge transfer efficiency and photocatalytic performance. The best HER performance is found to be as high as 122 μmol/h/g_{cat} with the Chl-3@$Ti_3C_2T_x$ composite. This work leads the direction in synthesizing Chls in Chl/MXene hybrid structure suitable for highly efficient photocatalytic HER.

Keywords: aggregates materials, chlorophyll derivatives, energy migration, hydrogen evolution reaction, $Ti_3C_2T_x$ MXene

1. Introduction

With the rapid development of global economy increasing and industrialization, the

huge demand for sustainable energy will become one of the most important problems affecting human survival and development in the near future [1,2]. Due to the limited resources of non-renewable fossil fuels such as coal, oil and natural gas, finding new green energies has become an urgent challenge. As a kind of abundant, clean and renewable energy, solar energy has been considered as one of the most important potential candidates to meet the demand of energy consumption [3,4]. Solar-driven photocatalytic water splitting for hydrogen evolution is one of the most promising strategies to convert solar energy into chemical energy. In the past decades, extensive investigations have been carried out to explore various semiconductor photocatalysts for the hydrogen evolution reaction (HER), for instance, TiO_2 [5,6], CoO [7], MoS_2 [8], C_3N_4 [9-12] and so on. However, most of the photocatalysts reported so far showed poor performances for HER, mainly due to the poor light absorption, high recombination rate of photo-induced charge carriers and insufficient reactive sites on the catalyst surface.

Natural photosynthesis has evolved for billions of years, chlorophylls (Chls) are the most abundant natural pigments on the earth and play key roles in light harvesting as well as energy/electron-transfer in natural photosynthetic systems [13,14]. Compared with other semiconductor photocatalysts, Chls are more promising for excellent photochemical and photophysical properties. Specifically, (i) Chls and their derivatives have excellent solar absorption property, covering an absorption spectrum from visible to near infrared region [15], (ii) can form aggregates to more efficiently capture sunlight and transfer charges compared with their monomers [16], (iii) can be easily synthesized from naturally abundant precursors widespread in green plants [17] and (iv) their chemical and physical properties are tunable through molecular engineering [18,19]. Because of their excellent optoelectronic properties, a series of investigations have been employed in solar cells [20], energy storage [21] and photocatalytic hydrogen evolution

[22-24]. Compared with other semiconductor photocatalysts employing artificial synthetic materials, natural Chls are low cost, environmentally friendly, easy to dispose, more abundant and less toxic. Therefore, Chls show great potential for photocatalytic HER systems. However, high recombination efficiency of photo-induced electron–hole pairs has hindered practical application of photocatalytic HER. A number of investigations have been implemented to improve photocatalytic activity, such as doping [25], structural engineering [26], co-catalyst loading and metal decoration [27]. Among them, co-catalyst loading is an effective approach to achieve a highly efficient HER. However, co-catalysts in conventional photocatalytic systems are usually composed of graphene[28], transition metal sulfides[29], metal nanoparticles[30] and other carbon materials[31], which dramatically increases the cost of photocatalytic systems; therefore high-efficiency and low cost co-catalysts have been urgently desired for the large-scale commercialization [32-34].

MXenes are a new family of 2D materials that were first reported in 2011 with the chemical formula $M_{n+1}X_nT_x$, where M represents the transition metal element (Ti, V, Nb, Ta or Mo), X is C and/or N, T_x is a surface terminating group such as -O, -F and -OH and n is between 1 and 3 [35-38]. Due to their remarkably electrochemical properties, MXenes have been widely studied for a variety of applications, such as energy storage [39,40], photovoltaic devices [41], catalysis [42-45] and so on. As the most widely studied MXenes to date, $Ti_3C_2T_x$ has been reported as an efficient co-catalyst for high-efficiently photocatalytic activity[46-48], which is mainly attributed to $Ti_3C_2T_x$ hydrophilic groups (-OH and -O) that can easily construct strong connection with various semiconductors. Furthermore, $Ti_3C_2T_x$ MXene has an excellent electronic conductivity that facilitate photo-induced charge transfer from the semiconductor to the $Ti_3C_2T_x$ MXene [49]. As discussed above, $Ti_3C_2T_x$ MXene with these outstanding

properties is expected to become a promising co-catalyst for HER.

In this work, we employed three Chls as photocatalysts, namely, zinc methyl 3-devinyl-3-hydroxymethyl-pyropheophorbide-*a* (Chl-1), zinc dodecyl 3-devinyl-3-hydroxymethyl-pyropheophorbide-*a* (Chl-2) and zinc dodecyl 13^1-deoxo-3-devinyl-13^1-dicyanomethylene-3-hydroxymethyl-pyropheophorbide-*a* (Chl-3), that are combined with $Ti_3C_2T_x$ MXene as a co-catalyst for photocatalytic activity study under the visible light irradiation. We found that the Chl-3@$Ti_3C_2T_x$ composite photocatalyst exhibited a much higher photocatalytic performance (122 μmol/h/g) than Chl-1@$Ti_3C_2T_x$ photocatalyst (20 μmol/h/g) and Chl-2@$Ti_3C_2T_x$ photocatalyst (48 μmol/h/g). Such a significant enhancement in the photocatalytic activity was further studied in terms of electronic absorption spectra, electrochemical impedance spectroscopy (EIS) and transient photocurrent (TPC) responses.

2. Experimental section

2.1 Synthesis of Chl derivatives and $Ti_3C_2T_x$ MXene

Chl-1, Chl-2 and Chl-3 were prepared as previously reported [50-52]. $Ti_3C_2T_x$ MXene was fabricated by etching Ti_3AlC_2 (Forsman, 98%) in 49% HF as follows. 49% HF (20 mL) was stirred at 300 rpm, and Ti_3AlC_2 (2 g) were slowly added at room temperature for 24 h. After that, the obtained solution was washed and centrifuged with deionized water several times until neutral pH was reached, then the $Ti_3C_2T_x$ sediment was collected after discarding the supernatant. Finally, $Ti_3C_2T_x$ MXene was dried in vacuum oven at 50 °C for 12 h.

2.2 Preparation of Chls@$Ti_3C_2T_x$ composites

$Ti_3C_2T_x$ (3 mg) and a certain amount of Chl-1 were dissolved in tetrahydrofuran

(THF). The mass ratios of Chl-1 to $Ti_3C_2T_x$ were 0.5% (15 μg), 2% (60 μg), 4% (120 μg), or 8% (240 μg). The Chl-1@$Ti_3C_2T_x$ mixture was stirred at room temperature for 12 h until dry. Then, Chl-1@$Ti_3C_2T_x$ composite was successfully prepared. Chl-2@$Ti_3C_2T_x$ and Chl-3@$Ti_3C_2T_x$ composites were synthesized by the same method as Chl-1@$Ti_3C_2T_x$.

2.3 Characterization

To characterize Chl-1, Chl-2, Chl-3, $Ti_3C_2T_x$ and their composites, an X-ray diffraction (XRD, D8 Advance, Bruker) was operated at 40 kV and 200 mA with Cu Kα radiation (λ = 0.15406 nm). Scanning electron microscopy (SEM, SU8000, Hitachi) was used to observe the morphology of the samples. The energy-dispersive X-ray spectroscopy (EDS, Magellan400) mapping was measured to investigate the distribution of element. Electronic absorption spectra of samples were measured with a UV-vis spectrometer (UV-3600, Shimadzu). The steady-state photoluminescence (PL) was measured on a Shimadzu RF-6000 spectrophotometer. PL decay profiles were obtained on a PL spectrometer (FLS 920, Edinburgh Instruments).

2.4 Photocatalytic activity measurements

Photocatalytic H_2 evolution was measured under a 300 W Xenon lamp (PLS-SXE 300, Beijing Perfectlight Technology Co., Ltd) with the light intensity of 100 mW/cm^2. A 6 mL photoreactor and a cut-off filter (usually λ > 420 nm) were used. Chl-n@$Ti_3C_2T_x$ photocatalyst composite (3 mg) was added in an aqueous 55 mM ascorbic acid (AA) solution (3 mL). The mixture was sonicated for 5 min before light irradiation to fully disperse the composite. Argon was purged to remove oxygen in the solution and the reactor for 10 min. The reactants were continuously stirred under

irradiation of visible-to-near infrared light ($\lambda > 420$ nm). The hydrogen production was measured after the 6 h by a gas chromatograph (SP-3420A, Beijing Beifen-Ruili Analytical Instrument) with a thermal conductivity detector. The average values were obtained by five independent experiments. The carrier gas was argon and the column contained 5 Å molecular sieves.

2.5 Photoelectrochemical activity test

EIS measurements ranging from 0.1 Hz to 100 kHz were carried out with an electrochemical workstation (Bio-Logic SAS) in a standard three-electrode system. The working electrode was prepared by ultrasonically dispersing the Chl-n@$Ti_3C_2T_x$ composite (10 mg) in a mixture of deionized water (250 μL), ethanol (250 μL) and Nafion solution (20 μL, Sigma-Aldrich, 5 wt%) for 5 min, then the dispersion (20 μL) was drop-coated at room temperature onto an ITO square substrate (2 cm^2). Ag/AgCl was used as the reference electrode and Pt plate was used as the counter electrode. The electrolyte was an aqueous 0.5 M Na_2SO_4 solution of AA (2 g/L). TPC response was measured in the same three-electrode system. A 300 W Xenon lamp with a cut-off filter ($\lambda > 420$ nm) was used as the light source. All measurements were conducted at room temperature.

3. Results and discussion

3.1 Characterization of structures and morphology

Figure 1 shows the chemical structures of Chl-1, Chl-2 and Chl-3 used in the MXenes-based photocatalysts, which were prepared according to previously reported procedures. [50-52] These Chl-n (n = 1~3) have commonly a cyclic tetrapyrrole as its

framework, a hydroxymethyl group at the C3-position and zinc atom as the macrocyclic central metal. In addition, their molecular structures are partially different in the C13- and C17-substituents of the chlorin macrocycle. Chl-1 has carbonyl group at the C13-position and methyl group as the C17-propionate residue. In contrast with methyl ester Chl-1, Chl-2 has a long dodecyl chain as the esterifying group, which is favorable to its solubility and stability [53]. Comparing with ketone Chl-2, Chl-3 has a dicyanomethylene group at the 13^1-position, which contributes to its bipolar characteristic. It is worth mentioning that the 3^1-hydroxy group, central metal zinc atom and 13-carbonyl group along the molecular y-axis are of great significance for the self-assembly of Chl-1 and Chl-2 to form *J*-aggregates. In the case of Chl-3, the strongly electron-withdrawing 13^1-dicyanomethylene group produces a more electron-deficient zinc site and further extends the π-conjugated system. Thus, through the stronger coordination of 3^1-O to Zn and tighter π-stacking of chlorin chromophore, Chl-3 can also form *J*-type self-aggregate in spite of its lack of 13-carbonyl group [54].

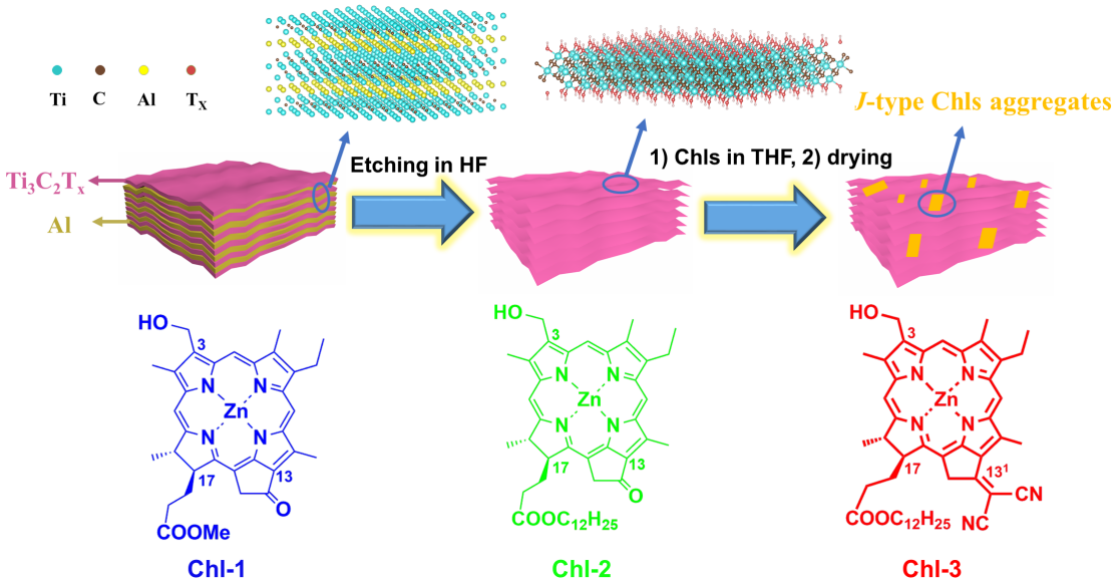

Fig. 1 Schematic diagram of the preparation process of Chl-n@$Ti_3C_2T_x$ composites (upper) and molecular structures of three Chl-1~3 (lower).

Figure 2 shows the XRD patterns of the raw materials and the Chl-n@$Ti_3C_2T_x$ composites studied herein. In Figure 2a, the (002) and (004) peaks of Ti_3AlC_2 moved toward lower angles in $Ti_3C_2T_x$ and the strongest peak at 39.0° of MAX phase disappeared, indicating that the Al layer was removed from Ti_3AlC_2. Figure 2b shows the XRD pattern of Chl-1 which displayed three typical peaks at 6.2°, 13.9° and 25.2°, as reported previously [22]. Both Chl-2 and Chl-3 displayed two typical peaks at 14.0° and 25.6°, as represented in Figures 2c and 2d. Both the characteristic peaks of $Ti_3C_2T_x$ and Chl-n can be observed in the XRD patterns of the resulting composites Chl-1@$Ti_3C_2T_x$, Chl-2@$Ti_3C_2T_x$ and Chl-3@$Ti_3C_2T_x$. No new XRD peak is generated in all the composites, indicating that the interaction of Chl-n with $Ti_3C_2T_x$ is based on their physical contacts rather than chemically bonding [22].

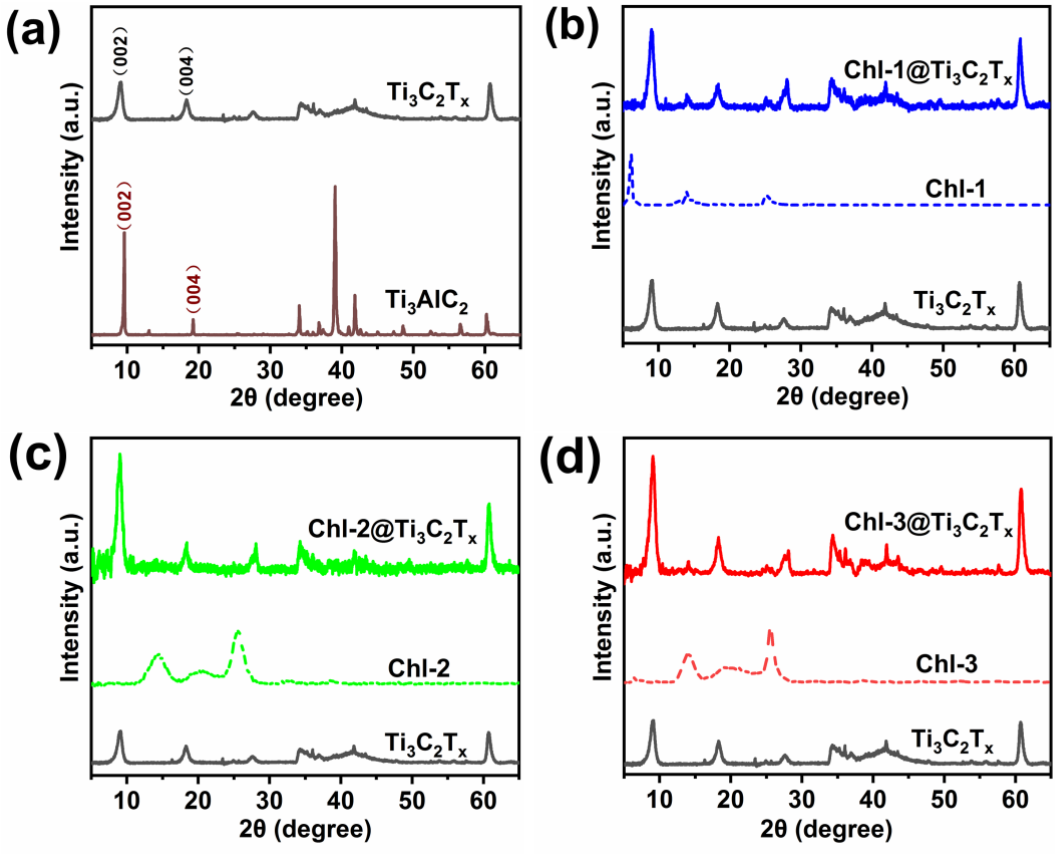

Fig. 2 XRD patterns of (a) Ti_3AlC_2, $Ti_3C_2T_x$, (b) $Ti_3C_2T_x$, Chl-1, Chl-1@$Ti_3C_2T_x$, (c) $Ti_3C_2T_x$, Chl-2, Chl-2@$Ti_3C_2T_x$ and (d) $Ti_3C_2T_x$, Chl-3, Chl-3@$Ti_3C_2T_x$.

The morphological characteristics of the Chl-n@$Ti_3C_2T_x$ composites were shown in the field emission SEM images (Figure 3). As shown in Figures 3a-c, the typical 2D nanosheet accordion-like structure of HF-etched $Ti_3C_2T_x$ is clearly observed, and no other significant change is observed. Besides this, the Chl-aggregates are unrecognizable through SEM image, suggesting that Chl-n form relatively small aggregates on the surface of $Ti_3C_2T_x$. The EDS images (Figures 3d-f) further display the distribution of Chl-n and $Ti_3C_2T_x$. The mappings revealed Ti and Zn elements, which is attributed to the Ti element of $Ti_3C_2T_x$ and Zn element of Chl-n, respectively. It could be seen that Ti and Zn elements were evenly distributed over the sample surface, indicating that Chl-n uniformly decorated the $Ti_3C_2T_x$ surface. Atomic force microscopy (AFM) images of Chl-n aggregates had been investigated previously [52,55], and the values of root-mean-square (RMS) reflect the surface roughness of Chl-n films. The RMS values follow the order of Chl-1 (21.76 nm) > Chl-2 (1.03 nm) ≈ Chl-3 (0.98 nm), showing that the surface roughness of Chl-2/3 with long dodecyl chain is much more smooth compared to that of Chl-1. This observation implies that Chl-2/3@$Ti_3C_2T_x$ composites give better interface contacts between Chls aggregates and $Ti_3C_2T_x$ surface. It should be noted that the intimate interface contact between Chls and $Ti_3C_2T_x$ is favorable for efficient transfer of charge carriers.

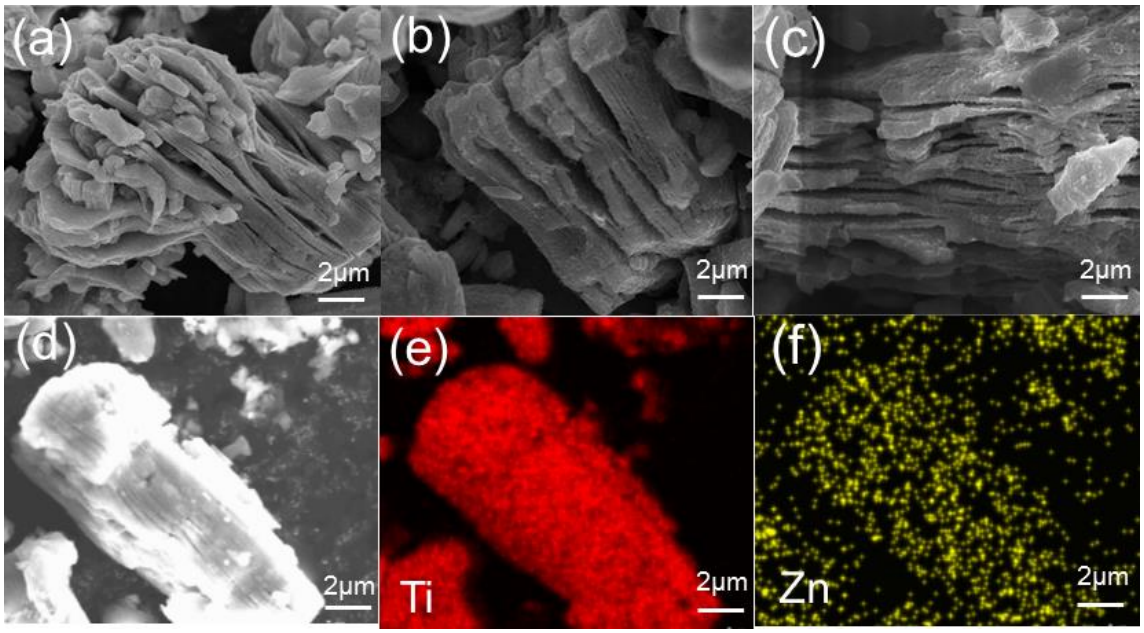

Fig. 3 SEM images of (a) Chl-1@$Ti_3C_2T_x$, (b) Chl-2@$Ti_3C_2T_x$, (c) Chl-3@$Ti_3C_2T_x$ and (d-f) EDS images of Chl-3@$Ti_3C_2T_x$.

3.2 Characterization of fluorescence spectra

In order to investigate the electron extraction process of different Chl-n@$Ti_3C_2T_x$ composites, the PL spectra of the Chls in solution and the Chl-n@$Ti_3C_2T_x$ composites were measured, as shown in Figures 4a-c. Strong PL signals of Chl-1, Chl-2 and Chl-3 were visible in THF at 660, 658 and 720 nm, respectively, after excitation at Soret maxima, suggesting that a large number of photo-excited charge carriers undergo recombination. The PL intensity remarkably decreased when $Ti_3C_2T_x$ was added into the solutions, indicating that the addition of $Ti_3C_2T_x$ remarkably enhanced electron-hole pair separation efficiency from the Chl-n to the $Ti_3C_2T_x$ and suppressed carrier recombination. In order to evaluate the quenching efficiency (QE) of Chls, following equation was employed: $QE\ (\%) = (1 - F/F_0) \times 100$, where F_0 and F represented the PL intensity of Chls before and after the addition of $Ti_3C_2T_x$, respectively [24]. The QE values of Chl-1/2/3@$Ti_3C_2T_x$ were calculated to be 48%/52%/61%, respectively. Thus,

Chl-3@$Ti_3C_2T_x$ possesses the strongest charge separation and transfer ability. In order to further investigate photo-generation carriers separation process, the PL decay profiles of Chls@$Ti_3C_2T_x$ were recorded in Figure 4d. The PL lifetimes of Chl-1/2/3@$Ti_3C_2T_x$ were 6.6/5.2/4.9 ns, respectively. The lifetime of Chl-3@$Ti_3C_2T_x$ was shorter than those of Chl-1/2@$Ti_3C_2T_x$, indicating that the Chl-3@$Ti_3C_2T_x$ had strongest ability of charge separation. These results also support the advantage of Chl-3@$Ti_3C_2T_x$, of which photogenerated carrier separation and transfer efficiency are higher than those of Chl-1/2@$Ti_3C_2T_x$, consistent with the results of steady-state PL spectra.

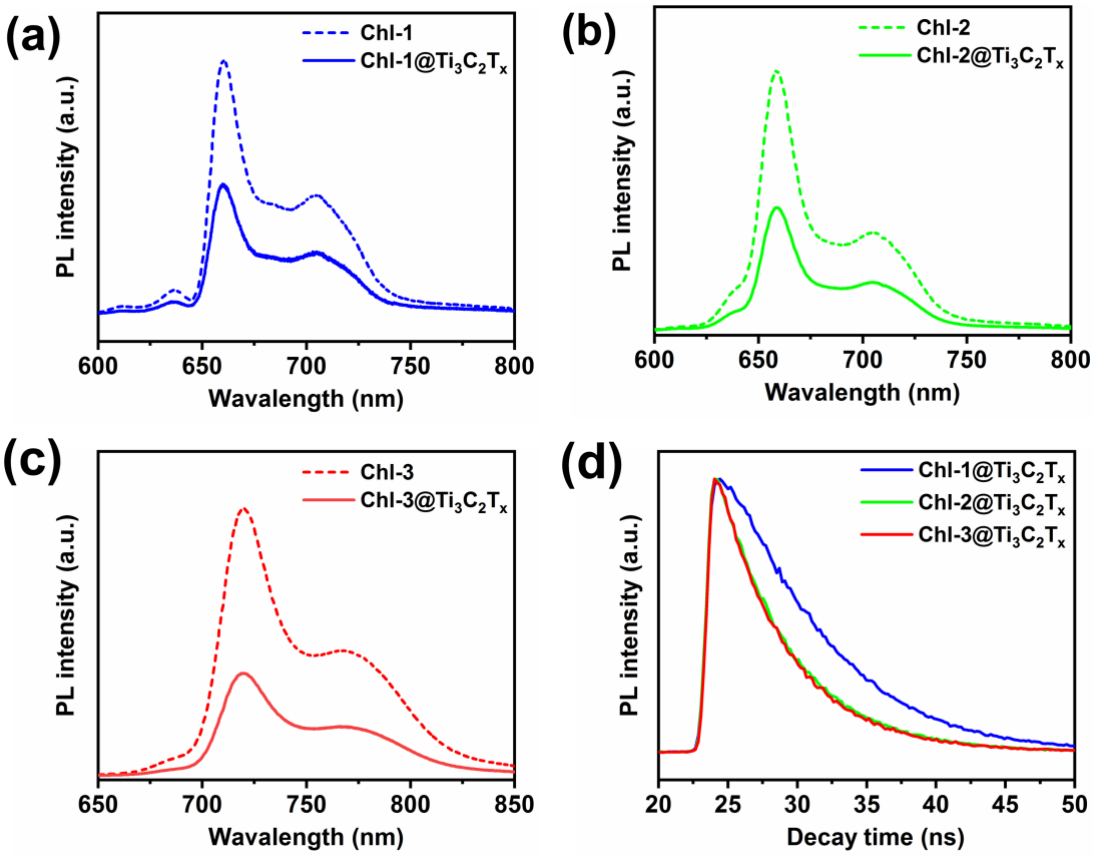

Fig. 4 (a-c) PL spectra of the Chl-1, Chl-2, Chl-3 in solution and their composites excited at 436, 433 and 463 nm, respectively and (d) PL decay profiles of their composites.

3.3 Electronic absorption characterization

The light absorption characteristics of the composites were recorded in electronic absorption spectra. As previously reported, $Ti_3C_2T_x$ had no significant absorption peak due to its metallic property [56]. The absorption spectra of Chl-n dissolved in THF and Chls@$Ti_3C_2T_x$ were illustrated in Figure 5a. The absorption spectra of Chl-n@$Ti_3C_2T_x$ composites showed obvious red-shifted and broader Soret and redmost (Q_y) absorption bands, compared with the corresponding Chl-n in solution. Compared with the location of Q_y absorption peak of Chl-1 positioned at 647 nm, the Q_y peak of Chl-1@$Ti_3C_2T_x$ composite was located at 720 nm, which displayed an evident red shift and broadening. It indicates that Chl-1 can self-assemble to form *J*-type self-aggregates when physical adsorption process is applied, which would promote the charge transfer in aggregates [57,58]. Similarly, for Chl-2 and Chl-3, the Q_y absorption peaks undergo significant red shifts and broadening, after deposition on $Ti_3C_2T_x$, i.e., the Q_y peaks shifted from 647 (Chl-2) to 735 nm (Chl-2@$Ti_3C_2T_x$) and from 697 (Chl-3) to 814 nm (Chl-3@$Ti_3C_2T_x$). The red shifts in their absorption spectra are attributed to the *J*-aggregation by intermolecular π-π stacking. In addition, Chl-3@$Ti_3C_2T_x$ showed a more red-shifted Q_y peak and a broader absorption band than the others, following the order of Chl-3@$Ti_3C_2T_x$ > Chl-2@$Ti_3C_2T_x$ > Chl-1@$Ti_3C_2T_x$. The larger red shift of the Q_y band indicates the stronger *J*-aggregation and the higher state of the aggregates which determine the charge transfer capability of Chl-n. Chl-1@$Ti_3C_2T_x$, Chl-2@$Ti_3C_2T_x$ and Chl-3@$Ti_3C_2T_x$ were all suitable for HER, and the Chl-3@$Ti_3C_2T_x$ composite demonstrated more excellent light-harvesting property than the others.

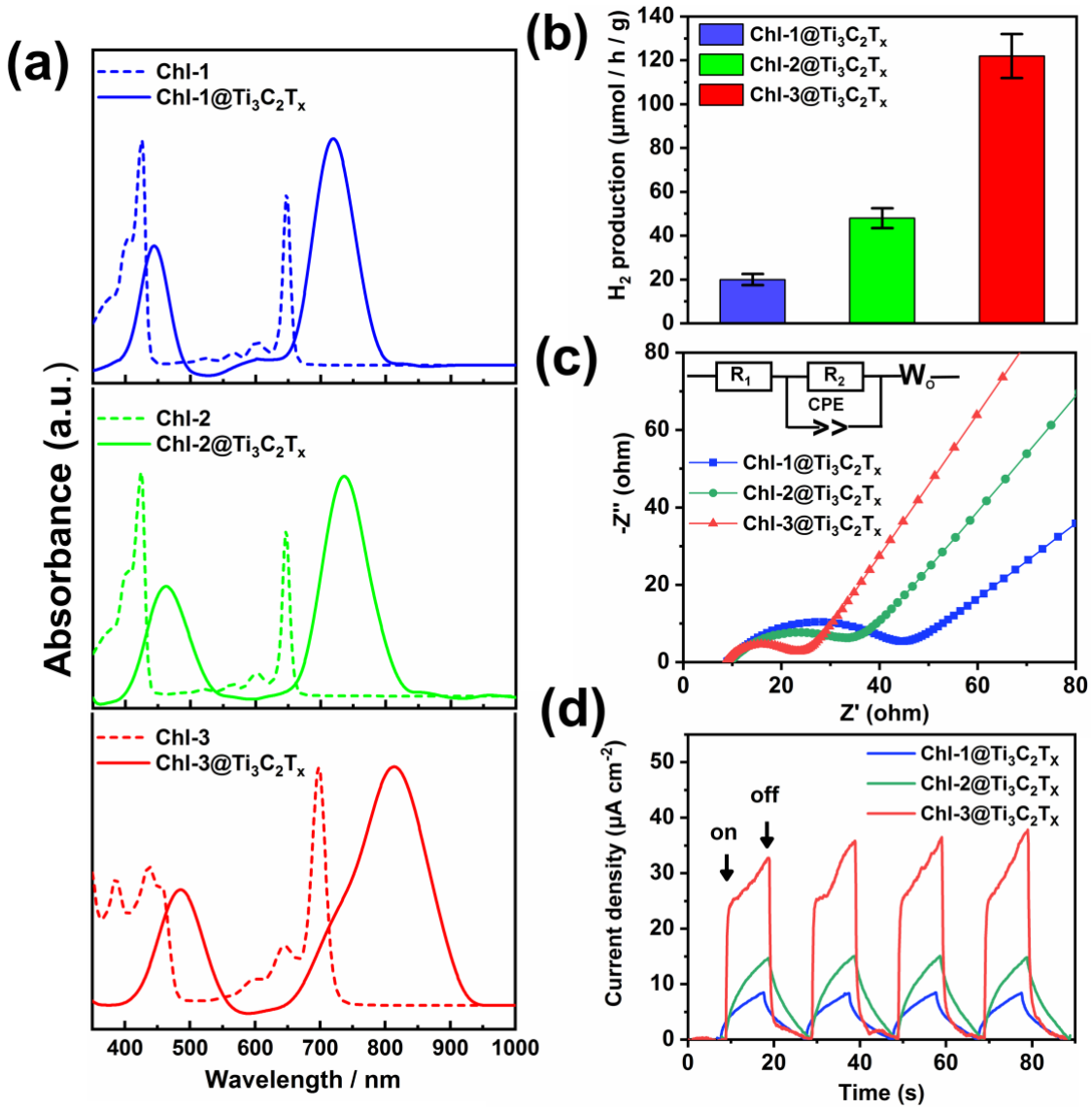

Fig. 5 (a) Electronic absorption spectra of the three Chl-n in solution and their composites. (b) Hydrogen production, (c) EIS Nyquist plots and (d) TPC responses of Chl-1@$Ti_3C_2T_x$, Chl-2@$Ti_3C_2T_x$ and Chl-3@$Ti_3C_2T_x$.

3.4 Photocatalytic performance of Chl-n@$Ti_3C_2T_x$ composites

These Chl-n@$Ti_3C_2T_x$ composites as the visible light photocatalysts were employed for water splitting. The optimization of mass ratio of Chls in the composites for photocatalytic hydrogen production were recorded and shown in Figure S1. Figure 5b displays the optimized photocatalytic performances of Chl-1@$Ti_3C_2T_x$,

Chl-2@$Ti_3C_2T_x$ and Chl-3@$Ti_3C_2T_x$ composites ($\lambda > 420$ nm). It could be found that the hydrogen production of Chl-1@$Ti_3C_2T_x$ was merely 20 μmol/h/g after optimizing the mass ratio of Chls to $Ti_3C_2T_x$ (see Figure S1). Likewise, the maximum hydrogen production performance of the Chl-2@$Ti_3C_2T_x$ composite presented a low hydrogen evolution rate (48 μmol/h/g). Impressively, the Chl-3@$Ti_3C_2T_x$ composite displayed a much superior hydrogen production performance than Chl-1@$Ti_3C_2T_x$ and Chl-2@$Ti_3C_2T_x$, which achieved as high as 122 μmol/h/g_{cat}. It reveals the Chl-3@$Ti_3C_2T_x$ composite owns the most excellent property for promoting the separation and transfer of photo-excited electron-hole pairs. This is mainly attributed to better interface contact, stronger aggregation states and greater light-harvesting capacity of Chl-3@$Ti_3C_2T_x$ composite, as discussed above.

To further explore the reasons of the improvement in performance, the charge transfer process was studied by EIS. Figure 5c shows the EIS Nyquist plots of Chls@$Ti_3C_2T_x$ composites, based on the corresponding equivalent model (inset). Here, R_1 represents the series resistance mainly related to the electrolyte solution, CPE and W_0 are the constant phase element and the Warburg impedance, respectively. R_2 is the interface charge transfer resistance between electrode and electrolyte. The semi-circle feature of a Nyquist plot defines the characteristic of charge transfer process and the semi-circle diameter represents the charge transfer resistance. The radius of the semi-circle of Chl-3@$Ti_3C_2T_x$ was smaller than those of Chl-1@$Ti_3C_2T_x$ and Chl-2@$Ti_3C_2T_x$, indicating a better electrical conductivity on the electrode surface and more efficient electron transfer from Chl-3 to $Ti_3C_2T_x$ upon excitation. The fitted resistance values are listed in Table S1. The R_2 value of each composite decreases in the order of Chl-1@$Ti_3C_2T_x$ > Chl-2@$Ti_3C_2T_x$ > Chl-3@$Ti_3C_2T_x$, implying the highest electron-hole pair separation efficiency for Chl-3@$Ti_3C_2T_x$.

Figure 5d shows the photocurrent–time response of Chl-1@$Ti_3C_2T_x$, Chl-2@$Ti_3C_2T_x$ and Chl-3@$Ti_3C_2T_x$ electrodes under Xe lamp illumination (λ > 420 nm) with repeatable on/off cycles. The intensity of the TPC response was employed to estimate the ability of photogenerated carrier separation and transfer efficiency from Chl-n to $Ti_3C_2T_x$. The Chl-1@$Ti_3C_2T_x$ composite displayed the lowest TPC response among all the composites due to the rapid recombination of photoexcited electron-hole pairs. A little increase in photocurrent intensity of Chl-2@$Ti_3C_2T_x$ suggests a better photogenerated carrier separation and transfer efficiency for Chl-2@$Ti_3C_2T_x$. The Chl-3@$Ti_3C_2T_x$ showed the largest photocurrent intensity, demonstrating that Chl-3@$Ti_3C_2T_x$ possessed the largest charge separation and transfer ability, which is in line with the above results.

As discussed above, the performance of Chl-n@$Ti_3C_2T_x$ composites in the HER systems is determined by surface roughness, ability of light-harvesting, aggregation states and electron transfer/recombination efficiency. The optimal performance of Chl-3@$Ti_3C_2T_x$ in the HER systems is based on these factors. First, the surface roughness of Chl-3 possessing the long dodecyl chain is low, which means Chl-3@$Ti_3C_2T_x$ composite has a better interface contact. Second, the more red-shifted and broader absorption spectra indicate the most excellent intrinsic ability of light harvesting for Chl-3@$Ti_3C_2T_x$. Third, both the PL spectra and their decay profiles indicate that Chl-3@$Ti_3C_2T_x$ composite had a higher electron-hole pair separation efficiency. Fourth, lower charge transfer resistance of Chl-3@$Ti_3C_2T_x$ demonstrated more efficient transfer of photogenerated electron-hole pairs from Chl-3 to $Ti_3C_2T_x$. Finally, Chl-3@$Ti_3C_2T_x$ showed the highest photogenerated electron-hole pairs separation ability, as reflected by the photocurrent responses. Intimate interface contact, strong capacity of light capture, suppression of electron-hole recombination,

improvement of carrier separation and reduction of charge transfer resistance, are all essential for a highly efficient photocatalytic HER.

3.5 Photoelectrochemical measurements

To clarify more clearly the effects of the $Ti_3C_2T_x$ deposited by different Chl derivatives Chl-n, the photocatalytic hydrogen evolution mechanism of the Chls@$Ti_3C_2T_x$ system was proposed as shown in Figure 6. Since the present Chl-n can self-assemble to form their large aggregates, the photo-excited state can be migrated inside their Chl-n aggregates. When the excitonic state reached near the $Ti_3C_2T_x$ surface, a charge separation occurs at the interface region. Since the LUMO levels of Chl-n are more positive than the work function of $Ti_3C_2T_x$ (-5.28 eV), photo-induced electrons can transfer from Chl-n to $Ti_3C_2T_x$ through ultrathin layered heterojunction. Subsequently, the photo-induced electrons accumulated on the surface of $Ti_3C_2T_x$ can react with two protons in an aqueous AA solution to generate H_2. Meanwhile, the photo-induced holes move inside the Chl-n self-aggregate to react with AA (a sacrificial agent) in a solid-solution interface. This special charges transfer pathway extends the distance between electrons and holes extremely, which will make the electron−hole pair separation more efficiently and thus suppress their recombination. As a result, the photocatalytic H_2 evolution efficiency can be greatly improved. At the same time, the oxidized Chl can be reduced by AA (-4.55 eV) to accomplish the cycle, so that the photocatalyst Chl accomplished to the regeneration of the ground state.

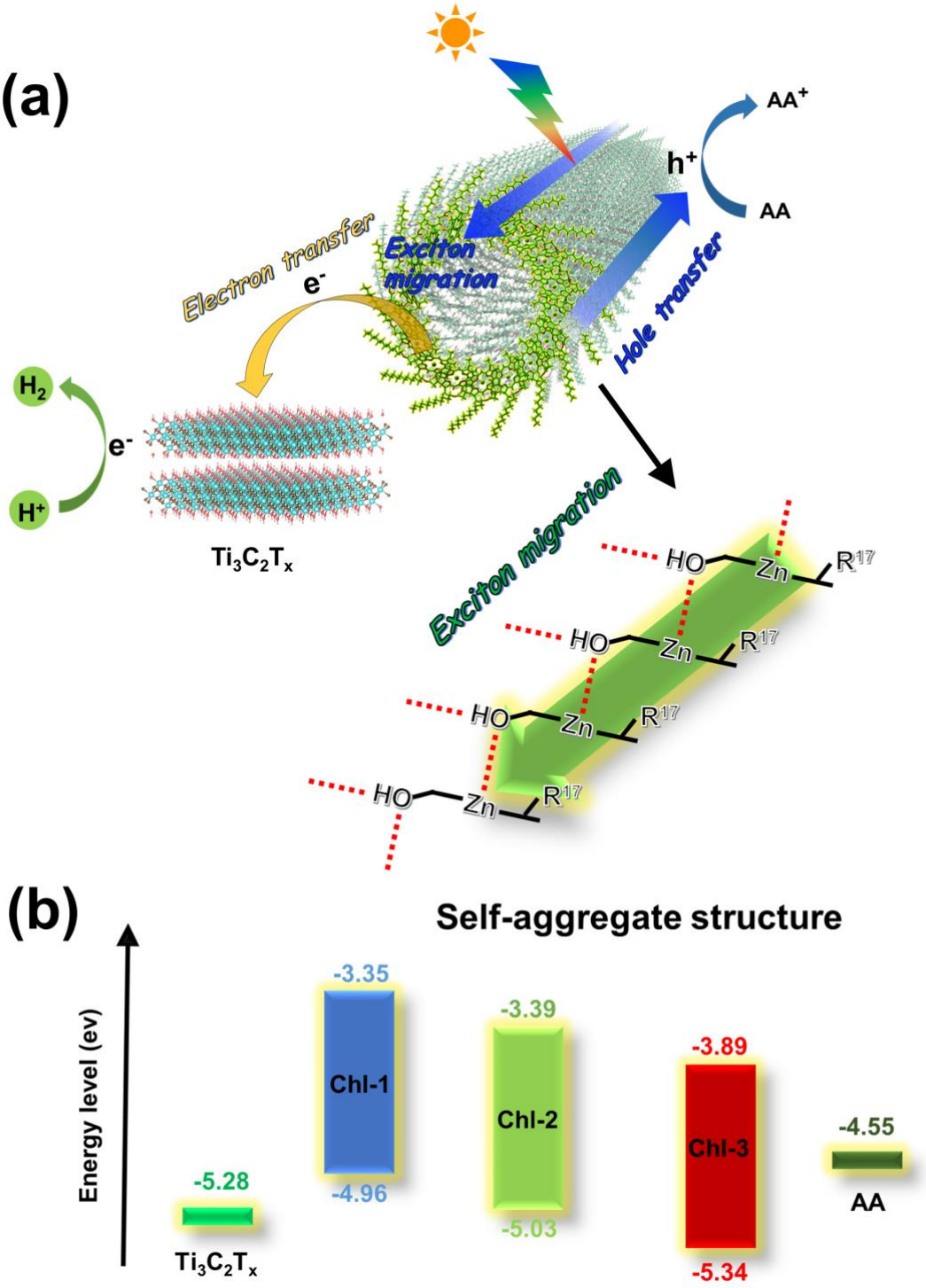

Fig. 6 (a) Schematic diagram of hydrogen production for Chl-n@$Ti_3C_2T_x$ composites under visible light irradiation and (b) energy-level diagram.

4. Conclusions

In summary, this work used three different Chl derivatives, Chl-n (n = 1~3) for the highly efficient photocatalytic H_2 evolution from water splitting. Meanwhile, the noble metal-free $Ti_3C_2T_x$ and the naturally abundant and environmentally friend Chls were employed as a co-catalyst and light absorbers, respectively. The Chl-n@$Ti_3C_2T_x$ photocatalysts were prepared by means of a simple deposition process. Chl-3@$Ti_3C_2T_x$ exhibited the highest H_2 evolution rate among the three Chls, due to its better interface contact, excellent inherent light-harvesting ability and higher electron-hole pair separation efficiency. The photocatalytic activity was optimized by changing the ratios of Chls over $Ti_3C_2T_x$, the optimal sample of Chl-3@$Ti_3C_2T_x$ presented the highest hydrogen production rate of 122 μmol/h/g_{cat} under visible light illumination ($\lambda > 420$ nm), which is much higher than those of Chl-1@$Ti_3C_2T_x$ (20 μmol/h/g) and Chl-2@$Ti_3C_2T_x$ (48 μmol/h/g). The combination of different Chl derivatives with 2D $Ti_3C_2T_x$ nanosheet for HER in this study opens up new perspectives in fabrication of structurally more favorable Chls-based semiconductors for the development of visible-light-active photocatalysts with a high efficiency.

Declaration of competing interest

The authors declare that they have no known competing financial interests or personal relationships that could have appeared to influence the work reported in this paper.

Author contribution statement

X.-F.Wang and Y. Li generated the idea and designed the experimental plan. Y. Li

performed the writing of the manuscript and the fabrication and characterization of the photocatalyst. Y. Liu, X. Sun and T. Zheng made some suggestions about data analysis. Y. Dall'Agnese and C. Dall'Agnese revised and made constructive suggestions on the manuscript. S. Sasaki and H. Tamiaki contributed to the synthesis of Chl-1, Chl-2 and Chl-3. X.-F.Wang provided related experimental conditions and participated in the technical discussions.

Acknowledgements

This work was supported by the National Natural Science Foundation of China (No. 11974129 to X.-F. W.) and "the Fundamental Research Funds for the Central Universities, Jilin University" and Japan Society for the Promotion of Science (JSPS) KAKENHI Grant Number JP17H06436 (to H.T.).

References

[1] Martin DJ, Liu G, Moniz SJ, Bi Y, Beale AM, Ye J, et al. Efficient visible driven photocatalyst, silver phosphate: performance, understanding and perspective. Chem Soc Rev 2015;44(21):7808-28.

[2] Lang X, Chen X, Zhao J. Heterogeneous visible light photocatalysis for selective organic transformations. Chem Soc Rev 2014;43(1):473-86.

[3] Lu X, Xie S, Yang H, Tong Y, Ji H. Photoelectrochemical hydrogen production from biomass derivatives and water. Chem Soc Rev 2014;43(22):7581-93.

[4] Ran J, Zhang J, Yu J, Jaroniec M, Qiao SZ. Earth-abundant cocatalysts for

semiconductor-based photocatalytic water splitting. Chem Soc Rev 2014;43(22):7787-812.

[5] Ma Y, Wang XL, Jia YS, Chen XB, Han HX, Li C. Titanium dioxide-based nanomaterials for photocatalytic fuel generations. Chem Rev 2014;114(19):9987-10043.

[6] Lang XJ, Ma WH, Chen CC, Ji HW, Zhao JC. Selective aerobic oxidation mediated by TiO_2 photocatalysis. Acc Chem Res 2014;47(2):355-63.

[7] Liao LB, Zhang QH, Su ZH, Zhao ZZ, Wang YN, Li Y, et al. Efficient solar water-splitting using a nanocrystalline CoO photocatalyst. Nat Nanotechnol 2014;9(1):69-73.

[8] Peng R, Liang LB, Hood ZD, Boulesbaa A, Puretzky A, Ievlev AV, et al. In-plane heterojunctions enable multiphasic two-dimensional (2D) MoS_2 nanosheets as efficient photocatalysts for hydrogen evolution from water reduction. ACS Catal 2016;6(10):6723-9.

[9] Cao SW, Yu JG. g-C_3N_4-based photocatalysts for hydrogen generation. J Phys Chem Lett 2014;5(12):2101-7.

[10] Ong WJ, Tan LL, Ng YH, Yong ST, Chai SP. Graphitic carbon nitride (g-C_3N_4)-based photocatalysts for artificial photosynthesis and environmental remediation: are we a step closer to achieving sustainability? Chem Rev 2016;116(12):7159-329.

[11] Zheng DD, Cao XN, Wang XC. Precise formation of a hollow carbon nitride structure with a Janus surface to promote water splitting by photoredox catalysis. Angew Chem Int Ed 2016;55(38):11512-6.

[12] Sun JH, Zhang JS, Zhang MW, Antonietti M, Fu XZ, Wang XC. Bioinspired hollow semiconductor nanospheres as photosynthetic nanoparticles. Nat Commun 2012;3:1139.

[13] Tamiaki H, Shibata R, Mizoguchi T. The 17-propionate function of (bacterio)chlorophylls: biological implication of their long esterifying chains in photosynthetic systems. Photochem Photobiol 2007;83(1):152-62.

[14] Ryan AA, Senge MO. How green is green chemistry? Chlorophylls as a bioresource from biorefineries and their commercial potential in medicine and photovoltaics. Photochem Photobiol Sci 2015;14(4):638-60.

[15] Duan SN, Zhou Q, Li AJ, Wang XF, Sasaki S-i, Tamiaki H. Semisynthetic chlorophyll derivatives toward solar energy applications. Sol RRL 2020;4(6):2000162.

[16] Li Y, Sasaki S, Tamiaki H, Liu CL, Song JX, Tian WJ, et al. Zinc chlorophyll aggregates as hole transporters for biocompatible, natural-photosynthesis-inspired solar cells. J Power Sources 2015;297:519-24.

[17] Sasaki S, Wang XF, Ikeuchi T, Tamiaki H. Synthesis of carboxylated chlorophylls and their application as functional materials. J Porphyrins Phthalocyanines 2015;19(3):517-26.

[18] Wang XF, Tamiaki H. Cyclic tetrapyrrole based molecules for dye-sensitized solar cells. Energy Environ Sci 2010;3(1):94-106.

[19] Tamiaki H, Kunieda M. Photochemistry of chlorophylls and their synthetic analogs. Handb Porphyrin Sci 2011;11:223-90.

[20] Li N, Dall'Agnese C, Zhao W, Duan S, Chen G, Sasaki S-i, et al. Bilayer

chlorophyll derivatives as efficient hole-transporting layers for perovskite solar cells. Mater Chem Front 2019;3(11):2357-62.

[21] Zhang C, Zhao W, Sasaki S-i, Tamiaki H, Wang X-F. A chlorophyll derivative-based bio-solar energy conversion and storage device. Electrochim Acta 2020;347:136283.

[22] Li Y, Chen X, Sun Y, Meng X, Dall'Agnese Y, Chen G, et al. Chlorosome-like molecular aggregation of chlorophyll derivative on $Ti_3C_2T_x$ MXene nanosheets for efficient noble metal-free photocatalytic hydrogen evolution. Adv Mater Interfaces 2020;7(8):1902080.

[23] Sun Y, Sun YL, Dall'Agnese C, Wang XF, Chen G, Kitao O, et al. Dyad sensitizer of chlorophyll with indoline dye for panchromatic photocatalytic hydrogen evolution. ACS Appl Energ Mater 2018;1(6):2813-20.

[24] Sun Y, Wang XF, Chen G, Zhan CH, Kitao O, Tamiaki H, et al. Near-infrared absorption carboxylated chlorophyll-*a* derivatives for biocompatible dye-sensitized hydrogen evolution. Int J Hydrogen Energy 2017;42(24):15731-8.

[25] Lin ZZ, Wang XC. Nanostructure engineering and doping of conjugated carbon nitride semiconductors for hydrogen photosynthesis. Angew Chem Int Ed 2013;52(6):1735-8.

[26] Zhang JY, Wang YH, Jin J, Zhang J, Lin Z, Huang F, et al. Efficient visible-light photocatalytic hydrogen evolution and enhanced photostability of core/shell CdS/g-C_3N_4 nanowires. ACS Appl Mater Interfaces 2013;5(20):10317-24.

[27] Bi LL, Meng DD, Bu QJ, Lin YH, Wang DJ, Xie TF. Electron acceptor of Ni

decorated porous carbon nitride applied in photocatalytic hydrogen production. Phys Chem Chem Phys 2016;18(46):31534-41.

[28] Tian HW, Liu M, Zheng WT. Constructing 2D graphitic carbon nitride nanosheets/layered MoS_2/graphene ternary nanojunction with enhanced photocatalytic activity. Appl Catal B 2018;225:468-76.

[29] Reddy DA, Park H, Ma R, Kumar DP, Lim M, Kim TK. Heterostructured WS_2-MoS_2 ultrathin nanosheets integrated on CdS nanorods to promote charge separation and migration and improve solar-driven photocatalytic hydrogen evolution. ChemSusChem 2017;10(7):1563-70.

[30] Li HF, Yu HT, Quan X, Chen S, Zhang YB. Uncovering the key role of the fermi level of the electron mediator in a Z-scheme photocatalyst by detecting the charge transfer process of WO_3-metal-gC_3N_4 (Metal = Cu, Ag, Au). ACS Appl Mater Interfaces 2016;8(3):2111-9.

[31] Wang Y, Liu XQ, Liu J, Han B, Hu XQ, Yang F, et al. Carbon quantum dot implanted graphite carbon nitride nanotubes: excellent charge separation and enhanced photocatalytic hydrogen evolution. Angew Chem Int Ed 2018;57(20):5765-71.

[32] Zhu Z, Lu ZY, Wang DD, Tang X, Yan YS, Shi WD, et al. Construction of high-dispersed Ag/Fe_3O_4/g-C_3N_4 photocatalyst by selective photo-deposition and improved photocatalytic activity. Appl Catal B 2016;182:115-22.

[33] Zhang GG, Lan ZA, Lin LH, Lin S, Wang XC. Overall water splitting by Pt/g-C_3N_4 photocatalysts without using sacrificial agents. Chem Sci 2016;7(5):3062-6.

[34] Gao GP, Jiao Y, Waclawik ER, Du AJ. Single atom (Pd/Pt) supported on graphitic

carbon nitride as an efficient photocatalyst for visible-light reduction of carbon dioxide. J Am Chem Soc 2016;138(19):6292-7.

[35] Naguib M, Kurtoglu M, Presser V, Lu J, Niu JJ, Heon M, et al. Two-dimensional nanocrystals produced by exfoliation of Ti_3AlC_2. Adv Mater 2011;23(37):4248-53.

[36] Naguib M, Mochalin VN, Barsoum MW, Gogotsi Y. 25th anniversary article: MXenes: a new family of two-dimensional materials. Adv Mater 2014;26(7):992-1005.

[37] Anasori B, Lukatskaya MR, Gogotsi Y. 2D metal carbides and nitrides (MXenes) for energy storage. Nat Rev Mater 2017;2(2):16098.

[38] Lukatskaya MR, Mashtalir O, Ren CE, Dall'Agnese Y, Rozier P, Taberna PL, et al. Cation intercalation and high volumetric capacitance of two-dimensional titanium carbide. Science 2013;341(6153):1502-5.

[39] Pan ZH, Cao F, Hu X, Ji XH. A facile method for synthesizing CuS decorated Ti_3C_2 MXene with enhanced performance for asymmetric supercapacitors. J Mater Chem A 2019;7(15):8984-92.

[40] Zhang CF, Anasori B, Seral-Ascaso A, Park SH, McEvoy N, Shmeliov A, et al. Transparent, flexible, and conductive 2D titanium carbide (MXene) films with high volumetric capacitance. Adv Mater 2017;29(36): 1702678.

[41] Yang L, Dall'Agnese C, Dall'Agnese Y, Chen G, Gao Y, Sanehira Y, et al. Surface-modified metallic $Ti_3C_2T_x$ MXene as electron transport layer for planar heterojunction perovskite solar cells. Adv Funct Mater 2019;29(46):1905694.

[42] Sun Y, Jin D, Sun Y, Meng X, Gao Y, Dall'Agnese Y, et al. g-C_3N_4/$Ti_3C_2T_x$ (MXenes) composite with oxidized surface groups for efficient photocatalytic hydrogen

evolution. J Mater Chem A 2018;6(19):9124-31.

[43] Li Y, Sun Y, Zheng T, Dall'Agnese Y, Dall'Agnese C, Meng X, et al. Chlorophyll-based organic heterojunction on $Ti_3C_2T_x$ MXene nanosheets for efficient hydrogen production. Chem Eur J 2021;27:5277-82.

[44] Xiao R, Zhao CX, Zou ZY, Chen ZP, Tian L, Xu HT, et al. In situ fabrication of 1D CdS nanorod/2D Ti_3C_2 MXene nanosheet Schottky heterojunction toward enhanced photocatalytic hydrogen evolution. Appl Catal B 2020;268:118382.

[45] Xu HT, Xiao R, Huang JR, Jiang Y, Zhao CX, Yang XF. In situ construction of protonated g-C_3N_4/Ti_3C_2 MXene schottky heterojunctions for efficient photocatalytic hydrogen production. Chinese J Catal 2021;42(1):107-14.

[46] Lu Y, Fan DQ, Chen ZP, Xiao WP, Cao CC, Yang XF. Anchoring Co_3O_4 nanoparticles on MXene for efficient electrocatalytic oxygen evolution. Sci Bull 2020;65(6):460-6.

[47] Zhao CX, Yang XF, Han CH, Xu JS. Sacrificial agent-free photocatalytic oxygen evolution from water splitting over Ag_3PO_4/MXene hybrids. Sol RRL 2020;4(8):1900434.

[48] Ding MY, Xiao R, Zhao CX, Bukhvalov D, Chen ZP, Xu HT, et al. Evidencing interfacial charge transfer in 2D CdS/2D MXene schottky heterojunctions toward high-efficiency photocatalytic hydrogen production. Sol RRL 2021;5(2):2000414.

[49] Ran JR, Gao GP, Li FT, Ma TY, Du AJ, Qiao SZ. Ti_3C_2 MXene co-catalyst on metal sulfide photo-absorbers for enhanced visible-light photocatalytic hydrogen production. Nat Commun 2017;8(1):13907.

[50] Tamiaki H, Amakawa M, Shimono Y, Tanikaga R, Holzwarth AR, Schaffner K. Synthetic zinc and magnesium chlorin aggregates as models for supramolecular antenna complexes in chlorosomes of green photosynthetic bacteria. Photochem Photobiol 1996;63:92-9.

[51] Shoji S, Hashishin T, Tamiaki H. Construction of chlorosomal rod self-aggregates in the solid state on any substrates from synthetic chlorophyll derivatives possessing an oligomethylene chain at the 17-propionate residue. Chem Eur J 2012;18(42):13331-41.

[52] Duan SN, Zhou Q, Dall'Agnese CX, Chen G, Wang XF, Tamiaki H, et al. Organic solar cells based on the aggregate of synthetic chlorophyll derivative with over 5% efficiency. Sol RRL 2019;3(12):1900203.

[53] Li MZ, Li N, Hu WD, Chen G, Sasaki S, Sakai K, et al. Effects of cyclic tetrapyrrole rings of aggregate-forming chlorophyll derivatives as hole-transporting materials on performance of perovskite solar cells. ACS Appl Energy Mater 2018;1(1):9-16.

[54] Tamiaki H, Kuno M, Kunieda M. Self-aggregation of a synthetic zinc chlorophyll derivative possessing a 13^1-dicyanomethylene group as a light-harvesting antenna model. Tetrahedron Lett 2014;55(17):2825-8.

[55] Li MZ, Li N, Chen G, Sasaki S, Miyasaka T, Tamiaki H, et al. Perovskite solar cells based on chlorophyll hole transporters: Dependence of aggregation and photovoltaic performance on aliphatic chains at C17-propionate residue. Dyes Pigm 2019;162:763-70.

[56] Lu Y, Yao MH, Zhou AG, Hu QK, Wang LB. Preparation and photocatalytic

performance of $Ti_3C_2/TiO_2/CuO$ ternary nanocomposites. J Nanomater 2017;5:1978764.

[57] Ogi S, Grzeszkiewicz C, Würthner F. Pathway complexity in the self-assembly of a zinc chlorin model system of natural bacteriochlorophyll J-aggregates. Chem Sci 2018;9(10):2768-73.

[58] Shoji S, Ogawa T, Hashishin T, Ogasawara S, Watanabe H, Usami H, et al. Nanotubes of biomimetic supramolecules constructed by synthetic metal chlorophyll derivatives. Nano Lett 2016;16(6):3650-4.